Lattice dynamics and structural transition of the hyperhoneycomb iridate β-Li_2IrO_3 investigated by high-pressure Raman scattering

Sungkyun Choi,[1,*] Heung-Sik Kim,[2,3] Hun-Ho Kim,[1] Aleksandra Krajewska,[1] Gideok Kim,[1] Matteo Minola,[1] Tomohiro Takayama,[1] Hidenori Takagi,[1] Kristjan Haule,[2] David Vanderbilt,[2] and Bernhard Keimer[1]

[1] *Max Planck Institute for Solid State Research, Heisenbergstrasse 1, 70569 Stuttgart, Germany*
[2] *Department of Physics and Astronomy, Rutgers University, Piscataway, New Jersey 08854-8019, USA*
[3] *Department of Physics, Kangwon National University, 1 Gangwondaehak-gil, Chuncheon-si, Gangwon-do 24341, Republic of Korea*

(Dated: September 20, 2019)

We report a polarized Raman scattering study of the lattice dynamics of β-Li_2IrO_3 under hydrostatic pressures up to 7.62 GPa. At ambient pressure, β-Li_2IrO_3 exhibits the hyperhoneycomb crystal structure and a magnetically ordered state of spin-orbit entangled $J_{\text{eff}} = 1/2$ moments that is strongly influenced by bond-directional (Kitaev) exchange interactions. At a critical pressure of ~ 4.1 GPa, the phonon spectrum changes abruptly, indicating a first-order transition to a monoclinic structure. A comparison to the phonon spectra obtained from density functional calculations shows reasonable overall agreement. The calculations also indicate that the high-pressure phase is a nonmagnetic insulator driven by the formation of Ir–Ir dimer bonds. Our results thus indicate a strong sensitivity of the electronic properties of β-Li_2IrO_3 to the pressure-induced structural transition.

I. INTRODUCTION

The effect of spin-orbit coupling (SOC) on the electronic structure of heavy transition metal compounds with $4d$ and $5d$ valence electrons has attracted great attention, especially in search and characterization of unprecedented electronic phases and their dynamics.[1] A prominent example is the Kitaev quantum spin liquid, which exhibits unconventional quantum entanglement and fractionalized excitations, in contrast to conventional magnetic ordering phenomena.[2]

The search for a physical realization of the Kitaev spin liquid has motivated an intense research effort on honeycomb-based lattices with edge-sharing IrO_6 (Ir^{4+}) or $RuCl_6$ (Ru^{3+}) octahedra. The strong SOC of the Ir or Ru ions gives rise to the formation of local $J_{\text{eff}} = 1/2$ moments and to bond-dependent Kitaev exchange interactions.[3,4] Candidates for Kitaev magnetism have also been identified in materials with three-dimensional lattice architectures.[5–7]

However, almost all known Kitaev-candidate materials – α-A_2IrO_3 (A=Na, Li),[8] β-Li_2IrO_3,[9] γ-Li_2IrO_3,[10] and α-$RuCl_3$[11] – appear to show long-range magnetic order (at least in the absence of external magnetic fields): zigzag antiferromagnetism for Na_2IrO_3[12–15] and α-$RuCl_3$,[16,17] and incommensurate counterrotating magnetic order for the Li_2IrO_3 family.[18–21] The appearance of these long-range magnetic orders is currently understood as a consequence of the presence of non-negligible additional exchange interactions such as second- or third-nearest-neighbor Heisenberg terms[7] or symmetric anisotropy interactions[22] in addition to the predominant Kitaev interaction.

To study and manipulate the subdominant exchange couplings and move closer to the realization of a Kitaev quantum spin liquid, a number of recent investigations has focused on the influence of lattice distortions (especially a trigonal distortion in honeycomb-lattice materials[23,24]). To this end, both external pressure and chemical methods such as hydrogen intercalation have been used to modify the lattice structure of various Kitaev materials.[25–39]

In particular, a recent high-pressure study of β-Li_2IrO_3 with x-ray diffraction found a signature of a structural transition from the orthorhombic structure at ambient pressure ($Fddd$ space group, No. 70, mmm point group)[9,18] to a lower-symmetry monoclinic structure ($C2/c$ space group, No. 15, $2/m$ point group)[31] around P ~ 4 GPa at room temperature, extended to a low temperature x-ray study.[32] Recently, similar structural transitions have been experimentally reported in α-$RuCl_3$[36] around 1 GPa, in α-Li_2IrO_3[27–29] around 3 GPa, and also theoretically predicted in Na_2IrO_3 around 40 GPa[40] (experimentally no structural transition was observed below 25 GPa[25]).

Investigations of the lattice dynamics under pressure yield information complementary to diffraction techniques, and can potentially provide insight into static and dynamic spin-lattice coupling. Optical spectroscopy has been recently used to study this relationship in several materials including Na_2IrO_3,[25] α-Li_2IrO_3,[27] and α-$RuCl_3$.[36]

However, pressure-dependent Raman scattering studies of Kitaev materials have rarely been reported; only α-$RuCl_3$ has been examined.[38] Having distinct selection rules for phonons, Raman scattering is a suitable tool for this purpose, with a high sensitivity to small structural modifications.[41] Moreover, it can capture Raman-active optical phonons with high energy resolution, which makes detailed analysis of the phonon energies possible even under pressure.

Among Kitaev materials, the β-Li_2IrO_3[9] compound can be a good choice due to its three-dimensional Ir network that is less prone to structural defects common in

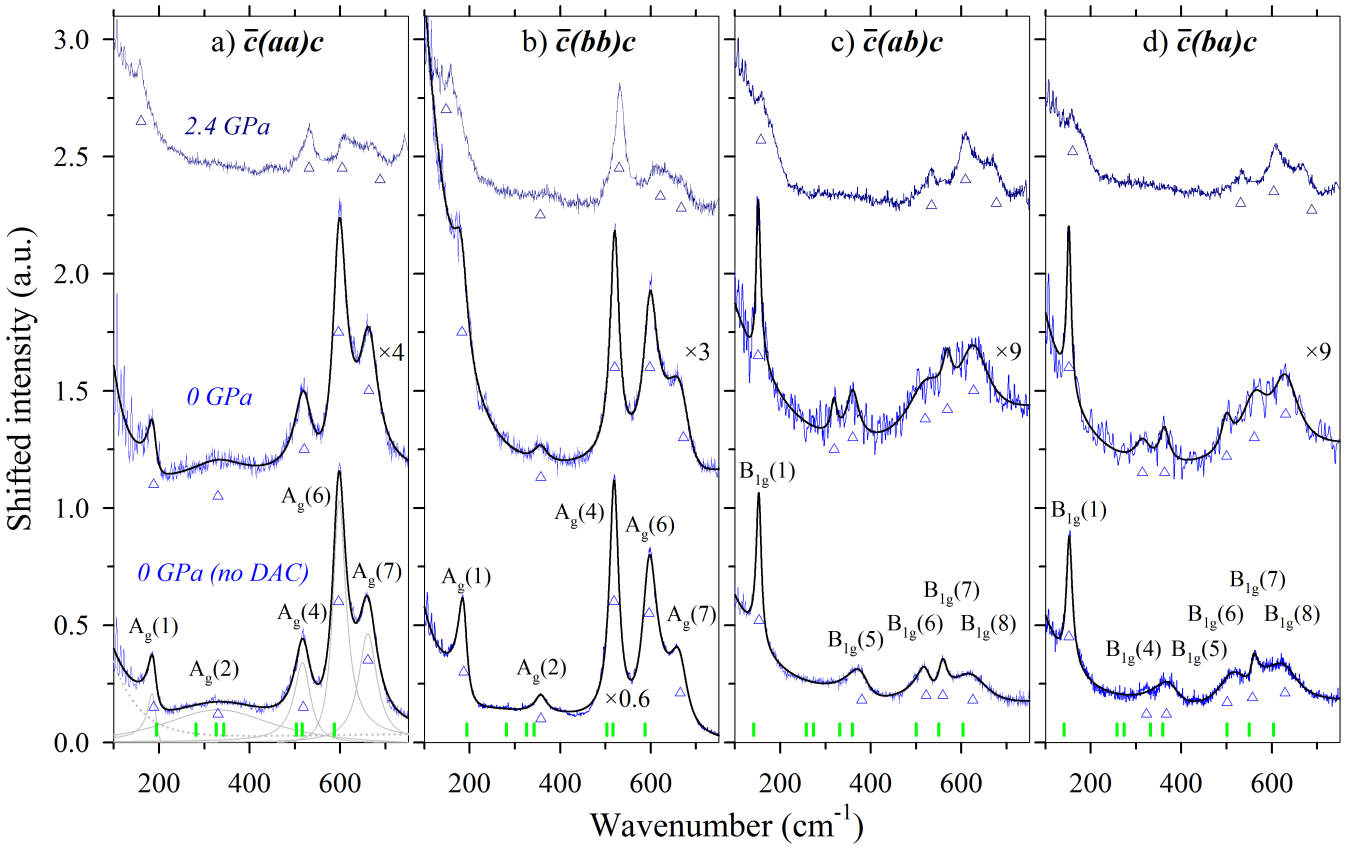

FIG. 1. (color online) Polarized Raman spectra at 0 GPa and 2.4 GPa with the green laser. Four polarization channels are shown: a) $\bar{c}(\boldsymbol{aa})\boldsymbol{c}$, b) $\bar{c}(\boldsymbol{bb})\boldsymbol{c}$, c) $\bar{c}(\boldsymbol{ab})\boldsymbol{c}$ and d) $\bar{c}(\boldsymbol{ba})\boldsymbol{c}$ defined at ambient pressure. Two ambient-pressure data (with and without Diamond Anvil Cell (DAC)) are compared with 2.4 GPa data. Blue lines are data and solid black lines are fitted curves (with a Fano profile). Upward triangular symbols indicate peak positions obtained from fits. Gray solid lines for the 0 GPa data (without DAC) in a) are decomposed contributions of each peak illustrated as a representative fit. The dotted line is the fitted background signal. The amplified 0 GPa data and the raw 2.4 GPa data were shifted vertically for more direct comparison. Calculated frequencies from density functional calculations are given with green vertical lines for comparison.

layered compounds such as α-A_2IrO_3 (A=Na, Li)[13,42] and α-$RuCl_3$.[16] In addition, because of its more ideal IrO_6 octahedral structure, β-Li_2IrO_3 is expected to be closer to the Kitaev spin liquid than its structural analogue γ-Li_2IrO_3.[10]

Here we have confirmed the existence of the recently reported structural transition by high-pressure Raman measurements on β-Li_2IrO_3 single crystals. We clearly observed the splitting and broadening of Raman-active phonon peaks and the development of multiple new Raman modes at high pressure, which are Raman hallmarks of a first-order structural transition to a lower crystal symmetry. At ambient pressure, polarization analysis allowed us to distinguish different Raman modes based on the Raman selection rules of a given crystal symmetry. The measured frequencies of Raman-active phonons both at ambient and high pressure were compared to those from *ab-initio* density functional theory and dynamical mean-field theory calculations. Our combined analysis suggests that the lower-symmetry monoclinic phase at high pressure originates from the dimerization of Ir ions, transforming the Ir atomic 5*d* orbitals into bonding and antibonding dimer states. This phase does not accommodate local $J_{\rm eff} = 1/2$ moments, indicating a delicate balance between magnetism and the intermetallic covalency. These conclusions are also consistent with a very recent neutron and resonant inelastic x-ray scattering study[43] characterizing the pressure-induced structural transition at room temperature.

The paper is organized as follows. Sections II and III describe details of the Raman scattering measurements and *ab-initio* calculations, respectively, followed by results and discussions in Section IV. Phonon spectra from high-pressure polarization-resolved Raman measurements on β-Li_2IrO_3 single crystals are presented in Section IV A. We then present and discuss computational results in Section IV B, followed by comparison between experimental and computational data in Section IV C. We summarize our conclusions in Section V.

II. EXPERIMENTAL DETAILS

Single crystals of β-Li_2IrO_3 were grown by a flux method[9]. We measured Raman spectra on more than 40 crystals, which were consistent with the previous result at ambient pressure.[44] We then screened crystals in terms of better signal-to-noise ratio, clearer surface morphology, and shinier surface to proceed with high-pressure Raman measurements. Raman data were also acquired from both green and red laser sources, revealing that the dominant Raman phonons in the spectra using incident green laser (514.5 nm) were stronger than those collected with the incident red laser (632.8 nm). The complete polarized Raman measurements were therefore carried out with the green laser [see Fig. 1 and 2] complemented by measurements with the red laser [see Fig. 3]. The former were fitted by Fano profiles[45] to extract the peak positions.

All measurements used a backscattering configuration and hereafter we use Porto's notation[46] to specify the experimental geometry.[47] With the backscattering geometry, we employed $\bar{\boldsymbol{c}}(\boldsymbol{aa})\boldsymbol{c}$, $\bar{\boldsymbol{c}}(\boldsymbol{bb})\boldsymbol{c}$, $\bar{\boldsymbol{c}}(\boldsymbol{ab})\boldsymbol{c}$, $\bar{\boldsymbol{c}}(\boldsymbol{ba})\boldsymbol{c}$ configurations to probe A_g, A_g, B_{1g} and B_{1g} modes at ambient pressure[44], where $\boldsymbol{a}$, $\boldsymbol{b}$ and $\boldsymbol{c}$ are the orthorhombic crystallographic axes. On the other hand, in the monoclinic structure at high pressure, all polarization geometries used in this study can only probe A_g^* phonons due to different Raman selection rules[47] (Table. II) from the orthorhombic symmetry at ambient pressure.

High-pressure Raman measurements with both laser lines were conducted with a mechanically-driven gasketed diamond anvil cell (Stuttgart-type). Diamond anvils had culet diameters of 0.4 mm and were of the ultra-low luminescence type. The stainless steel gaskets were preindented to 100 μm thickness and a hole of 175 μm diameter was drilled into each gasket by spark erosion. The hole was designed to ensure enough space for the thick β-Li_2IrO_3 single crystals. Several attempts for Raman measurements with thinner gaskets failed by breaking samples at intermediate pressures. A crystal that had been characterized by Raman scattering at ambient pressure was placed inside the hole of the gasket with a 4 : 1 methanol-ethanol liquid as a pressure medium to ensure hydrostatic pressure conditions up to 10.5 GPa.[48] Potential difficulties arising from increased viscosity of the pressure medium were avoided by keeping the pressure below 7.63 GPa. Pressures were measured by the ruby luminescence method with four ruby balls[49] spread spatially next to a β-Li_2IrO_3 crystal inside the gasket to accurately evaluate hydrostatic pressures, and were repeated before and after collecting the Raman data at each pressure, confirming only a small variation of pressure ($\Delta P \lesssim 0.1$ GPa).

III. COMPUTATIONAL DETAILS

In the *ab-initio* calculation, we used density functional theory (DFT) augmented by atomic spin-orbit coupling and on-site Coulomb interactions (DFT+SOC+U, hereafter DFT or DFT+U) where U indicates the electronic correlation. The Vienna *ab-initio* Simulation Package (VASP)[50,51] was employed, supplemented by WIEN2K[52] and DFT+Embedded DMFT Functional code (eDMFT)[53–55] calculations. Note that, unless specified, all DFT results presented include SOC and U within the DFT+U formalism. The PHONOPY package was employed to calculate the Γ-point phonon modes based on the relaxed orthorhombic and monoclinic structures.[56]

IV. RESULTS AND DISCUSSION

A. Raman experiments

Figure 1 presents Raman data on β-Li_2IrO_3[44] with phonon peaks identified. A group-theoretical analysis of the space group $Fddd$ reveals the following irreducible representations: $\Gamma = 7\ A_g\ (\boldsymbol{aa}, \boldsymbol{bb}, \boldsymbol{cc}) + 8\ B_{1g}\ (\boldsymbol{ab}) + 11\ B_{2g}\ (\boldsymbol{ac}) + 10\ B_{3g}\ (\boldsymbol{bc})$[44]. In the parallel (crossed) polarization geometries we employed, we observed 5 A_g (6 B_{1g}) modes as shown in Fig. 1 at ambient pressure. To identify artifacts from the pressure cell setup, the measurement were made without and with the Diamond Anvil Cell (DAC) at ambient pressure. We used Fano profiles for the fit (black lines), describing the data well as shown in Fig. 1. The peak positions extracted from these two data sets collected at both 0 GPa were nearly identical [also see overlapping empty and solid symbols in Figs. 2e-h) at 0 GPa]. The signal from the samples within the DAC became weaker due to the presence of the cell and the use of the lens with a smaller magnification (reduced from 50x to 20x) as seen from the comparison of the two data sets measured at 0 GPa in Figs. 1a-d).

When the pressure was increased to 2.4 GPa, no significant change in the Raman data was found except the hardening of the phonon frequencies (due to an increased effective spring constant between atoms by pressure). The number of peaks remained identical, confirming that the crystal structure remains unchanged up to this pressure.

Figure 2 shows Raman spectra as a function of pressure from 0 to 7.63 GPa with different geometries and polarizations. With a gradual increase of the pressure up to 3 GPa, almost all Raman phonon peaks hardened, except the $A_g(1)$ peak which softened from 188 cm^{-1} (at 0 Gpa) to 156 cm^{-1} (at 3 GPa) as shown in Figs. 2a-b). This particular $A_g(1)$ vibration (illustrated in Fig. 5c) became unstable as the material approached the critical pressure around 4.1 GPa (as will be discussed in Section IV C in more detail). Thus, this particular mode can be taken as an indicator of the structural instability.

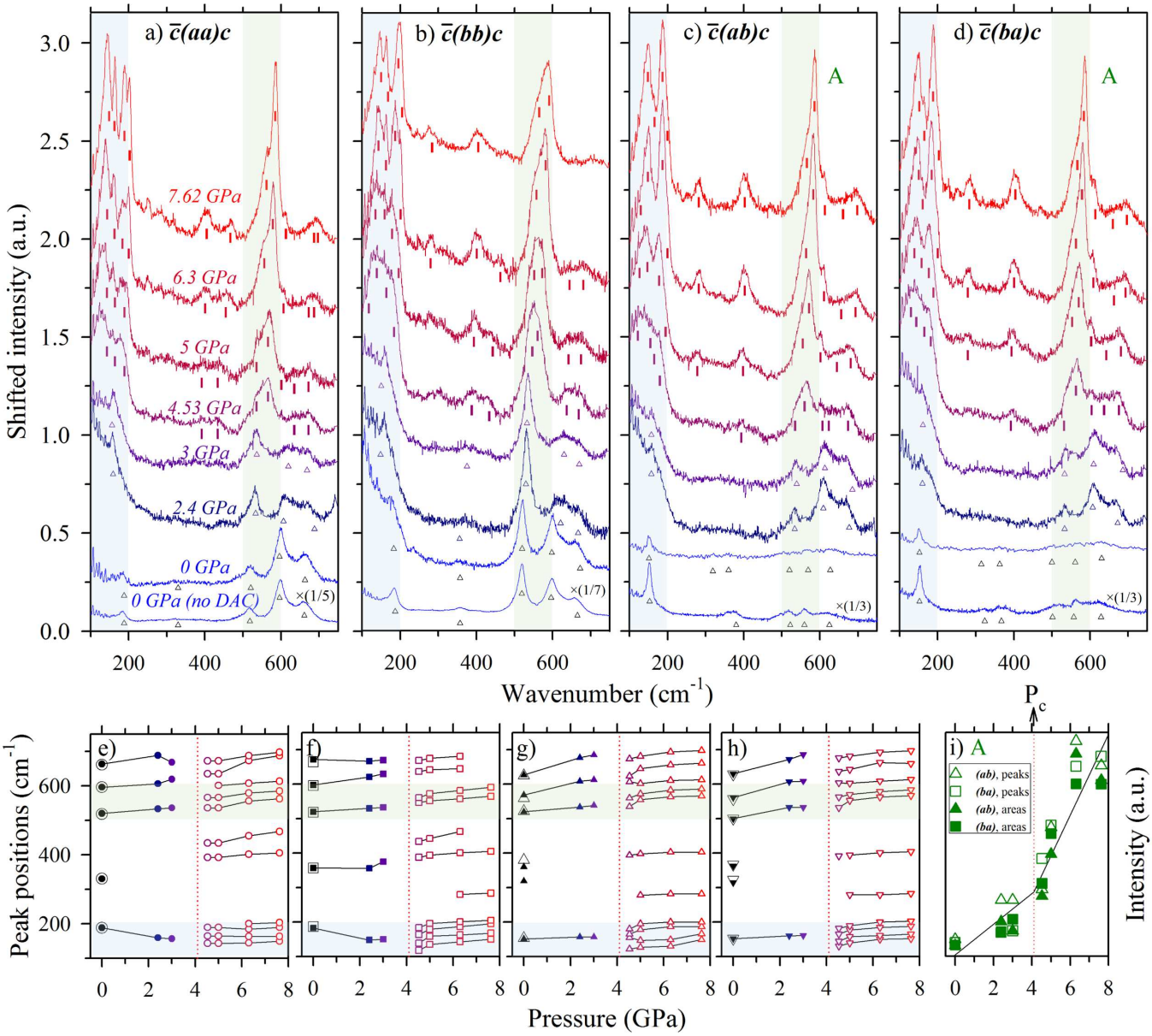

FIG. 2. (color online) Polarized Raman data as a function of pressure in four polarization geometries with the green laser: a) $\bar{c}(\boldsymbol{aa})\boldsymbol{c}$, b) $\bar{c}(\boldsymbol{bb})\boldsymbol{c}$, c) $\bar{c}(\boldsymbol{ab})\boldsymbol{c}$ and d) $\bar{c}(\boldsymbol{ba})\boldsymbol{c}$ defined at ambient pressure, corresponding A_g, A_g, B_{1g} and B_{1g} Raman-active modes, respectively. In the monoclinic structure at high pressure (for the 4.53 GPa data and above), only parallel Raman-polarized modes (A_g^*) were observed owing to the ($\boldsymbol{ab}$)-plane-oriented mounting using four polarization setups in this experiment. Note that the asterisk (*) symbol is included to remind that experimentally measured A_g^* phonons were not obtained from the exact backscattering condition at high pressures due to an inclined $\boldsymbol{c}$-axis in a monoclinic structure (β=106.777°)[31] relative to the backscattering direction used in the experimental setup: this level of inclination was tested with the in-plane rotation which did not practically alter Raman spectra at ambient pressure[47]. Triangular (vertical bar) symbols are extracted peak positions below (above) the critical pressure for the structural transition. Two regions of wavenumbers with the most dramatic change in the Raman spectra with pressure are emphasized with transparent blue and green rectangles at around 150 cm^{-1} and 550 cm^{-1}, respectively. The 0 GPa data without the DAC were scaled and all other data were vertically shifted for better comparison. e-h) Evolution of peak positions with pressure obtained from a-d). Bigger empty symbols from the 0 GPa data without the DAC are compared with solid symbols from the 0 GPa data with the DAC, confirming an excellent match of phonon frequencies. i) Two representations of summed intensities of Raman data highlighted as green boxes in c-d): summed peak intensities in between 500 and 600 cm^{-1} (empty symbols) and integrated areas between 550 and 600 cm^{-1} (filled symbols). The solid black line is a guide to the eyes and the vertically dotted red line marks the estimated critical pressure at about 4.1 GPa, which is also marked in e-h).

In Fig. 2, from 4.53 GPa and upwards, all phonon peaks broaden abruptly and then split into separate peaks at higher pressures, accompanying the appearance of new phonon peaks. The new modes are most clearly visible in the Raman spectra collected at the highest pressure presented (7.62 GPa); four clearly split peaks at about 150 cm^{-1} and two separate peaks at about 550 cm^{-1} are seen in Fig. 2a).

The spectral ranges most strongly affected by the structural transition are highlighted as blue and green shaded areas Figs. 2a-d). For a quantitative analysis, the spectra were fitted by Fano profiles and the fitted peak positions were marked by triangular (vertical bar) symbols before (after) the transition in Figs. 2a-d). The evolution of the peak positions as a function of pressure for four different geometries is plotted in Figs. 2e-h), revealing clear peak splitting and emergence of new peaks starting above the estimated critical pressure of 4.1 GPa (vertically dotted red lines).

To illustrate quantitatively the evolution of the lattice dynamics upon pressure, in Fig. 2i) we plotted the intensities of peaks around 550 cm^{-1} as a function of pressure. Results from two crossed polarization data sets ($\bar{c}(\boldsymbol{ab})\boldsymbol{c}$, $\bar{c}(\boldsymbol{ba})\boldsymbol{c}$) are shown using two methods: summed intensities of peaks from fits between 500 $\sim$ 600 cm^{-1} and integrated intensities between 550 $\sim$ 600 cm^{-1} illustrated as empty and filled symbols, respectively in Fig. 2i). The result demonstrates a kink at about 4.1 GPa, a Raman evidence for the first-order structural transition. This critical pressure for the transition is consistent from high-pressure x-ray[31] and neutron diffraction measurements.[43] With the Raman data, we chose the higher-wavenumber region (green rectangles in Figs. 2a-d)) to extract the critical pressure because this range of the energy window has weaker phonons at ambient pressure than those in the lower-wavenumber region (blue rectangles in Figs. 2a-d)), so that the change of the Raman spectra with pressure was most clearly captured.

To further confirm the pressure-induced Raman spectra, we also used a Raman setup with the red laser. Figure 3 presents the red Raman data with two polarizations, $\bar{c}(\boldsymbol{bb})\boldsymbol{c}$ and $\bar{c}(\boldsymbol{ab})\boldsymbol{c}$. In this measurement, a finer step of pressure was used with a short measurement time, revealing similar appearances of new Raman modes at high pressure. We observed the most pronounced changes in the Raman spectra for a similar range of wavenumbers, highlighted as a blue and green rectangle in Figs. 3a-b), analogous to the green data in Fig. 2a-d). The red Raman data is, thus, fully consistent with the green Raman data with a similar transition pressure. We point out that we better confirmed two Raman-active phonons at about 282 cm^{-1} and 402 cm^{-1} (marked by red downward arrows in Fig. 3), which were only weakly observed with the green laser shown in Figs. 2a-d).

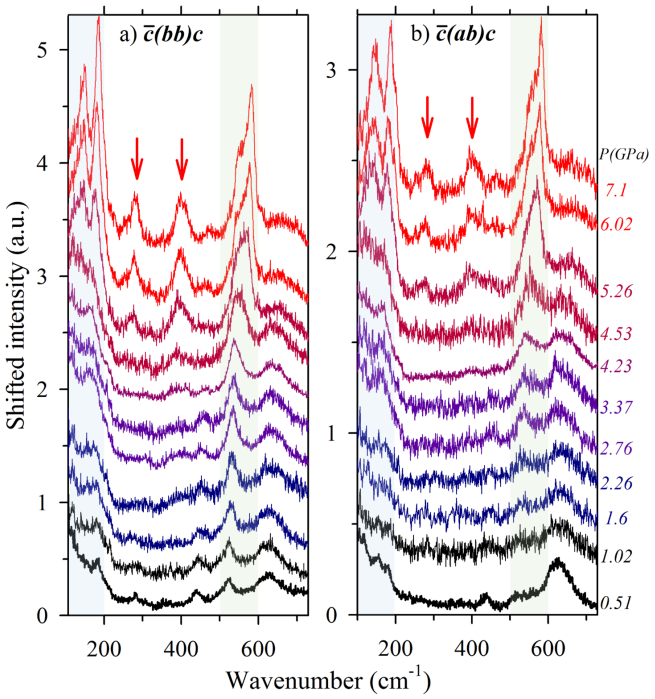

FIG. 3. (color online) Polarized Raman spectra with pressure with the red laser in a) $\bar{c}(\boldsymbol{bb})\boldsymbol{c}$ and b) $\bar{c}(\boldsymbol{ab})\boldsymbol{c}$ experimental geometry on a different crystal. Transparent blue and green rectangles are highlighted to indicate the energy windows, where the spectra changed significantly. The geometry of all crossed polarizations is $\bar{c}(\boldsymbol{ab})\boldsymbol{c}$ only except the 0.51 GPa data ($\bar{c}(\boldsymbol{ba})\boldsymbol{c}$ used). Measured pressures are noted in the right column next to the figure in GPa units. Note that both parallel and crossed polarization data prove Ag symmetric phonons at from 4.23 Gpa and above due to a Raman selection rule of the monoclinic structure at high pressures. Two red downward arrows emphasize strongly enhanced Raman signals with the red laser at about 282 and 402 cm^{-1}, which are only weakly observed with the green laser such as Fig. 2a) in the parallel polarization.

B. *Ab-initio* calculations

We now discuss our *ab-initio* DFT and DMFT calculation results on lattice structures and electronic properties with and without pressure. We first address DFT+U results on the phonon frequencies. To obtain accurate results, careful optimization of crystal structures in both orthorhombic and monoclinic symmetries (representing ambient and high-pressure conditions, respectively) is crucial. All the lattice parameters (*i.e.,* magnitudes of the Bravais lattice vectors and angles between them) and internal atomic coordinates were allowed to relax (see Fig. 4a)).

For the high-pressure conditions, the experimental monoclinic cell parameters[31] were first adopted as a trial structure, and then the unit cell shape and internal ionic coordinates (with the fixed cell volume) were optimized. No symmetry conditions were enforced during the op-

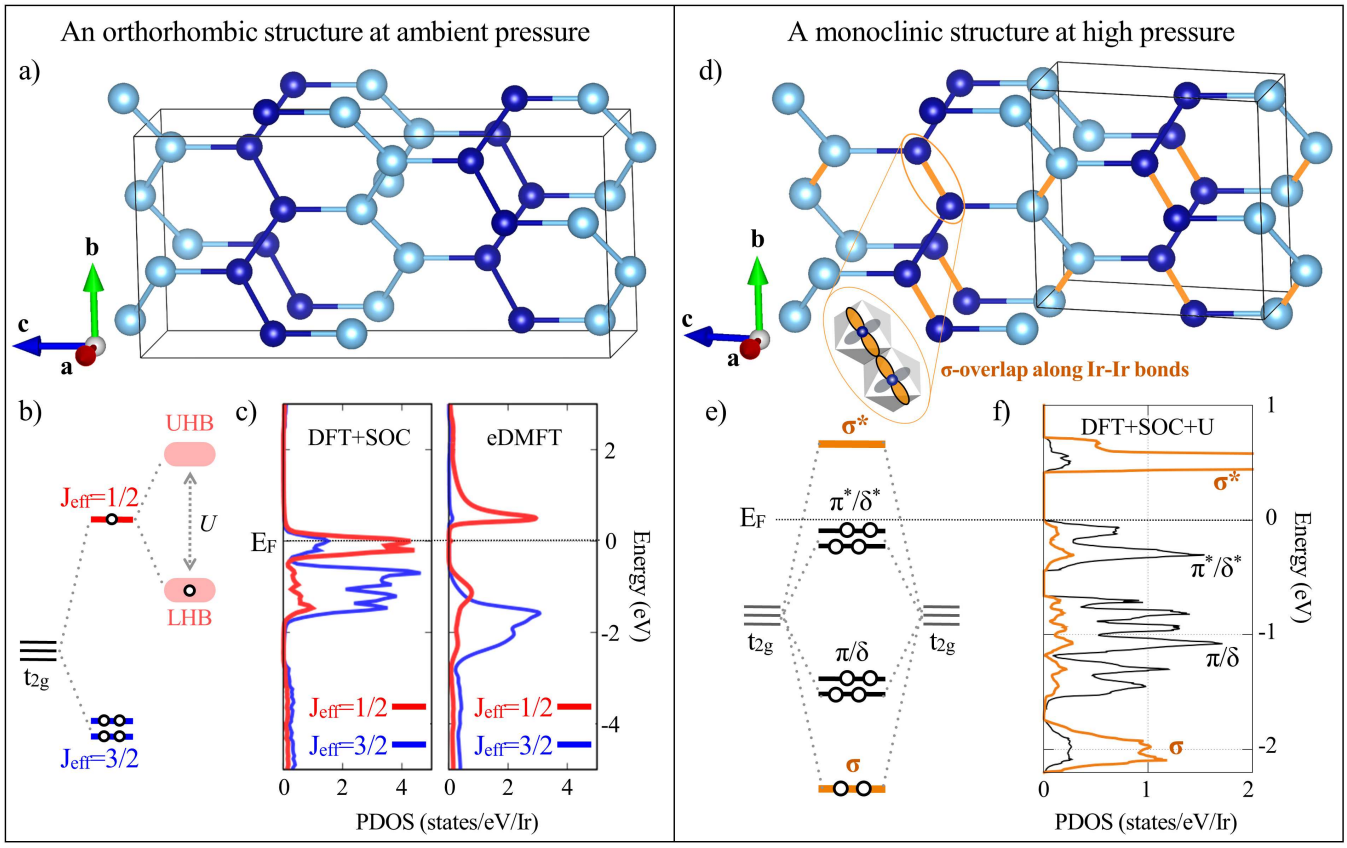

FIG. 4. (color online) a) (color online) a) Crystal structures of the relaxed orthorhombic β-Li_2IrO_3 structure at ambient pressure, where Ir sites forming nonparallel zigzag chains are depicted as dark and bright blue spheres (a relaxed DFT+U structure given in Table II in Ref. 47). The black solid box is the orthorhombic unit cell. b) A schematic energy diagram of the splitting between the $J_{\rm eff}$ = 1/2 and 3/2 states and a resulting Mott phase by the Coulomb interaction U. c) Comparison between the DFT+SOC (a left panel, neither U nor magnetism implemented) and eDMFT (a right panel) projected densities of states (PDOS) in the nonmagnetic phase. $J_{\rm eff}$ = 1/2 and 3/2 states are depicted in red and blue, respectively, where the opening of Hubbard gap and the enhancement of $J_{\rm eff}$ = 1/2 - 3/2 splitting is only seen in the eDMFT result. d) The distorted hyperhoneycomb lattice of Ir ions at high pressure in the optimized crystal structure in the calculation (a relaxed DFT+U+SOC structure given in Table III in Ref. 47), emphasizing with the dimerized Ir bonds (thick solid orange lines) with monoclinic axes. The black solid box is the monoclinic unit cell. Dark and bright blue balls are for iridium ions to describe a structural connectivity between zigzag chains. The inset shows a corresponding σ-overlapping t_{2g} orbitals driving the dimer formation. e) A schematic energy level representing the splitting of the Ir t_{2g} subspace and formation of the dimer bonding-antibonding orbitals. f) PDOS for Ir t_{2g} orbitals from the DFT+U result, showing the same energy level splitting given in e). The horizontal dotted line shows the Fermi energy, E_F. Lithium and oxygen ions are not visualized for a simplicity.

timizations. Our results reproduced the experimental lattice parameters and internal atomic coordinates reasonably well [see Supplemental Material[47] for tables]. It should be mentioned that the preconditioning is important to obtain reasonable crystal structures.

At ambient pressure, DFT calculations demonstrate the essential role of spin-orbit coupling and the on-site Coulomb interaction in maintaining the orthorhombic close-to-ideal hyperhoneycomb structure; the orthorhombic structure can be stabilized only when the Coulomb interaction and SOC are both incorporated in the DFT+U method (U = 2 eV for entire calculations) to obtain the magnetic and insulating phase.[57]

On the other hand, at high pressure, we obtain practically identical monoclinic structures with nonmagnetic (i.e., no local magnetic moments) dimerized Ir pairs regardless of the presence of SOC or U. This naturally implies an essential role of SOC and U for the orthorhombic crystal structure at ambient pressure, and in contrast its irrelevance in the high-pressure monoclinic structure. After the optimization, the phonon energies were obtained by diagonalizing the dynamical matrix.[58]

We now turn to calculations of the electronic structure. To gain additional insight into the electronic structures of the low- and high-pressure phases, we have performed a paramagnetic (PM) eDMFT calculation (T = 232 K, U = 5.0 eV, and J = 0.8 eV for Ir t_{2g} orbitals) to stabilize the PM Mott insulating phase, which consists of disordered

and localized magnetic moments instead of noninteracting bands in DFT-based calculations. The right panel of Figure 4c) presents the $J_{\rm eff}$-projected density of states (PDOS) from this eDMFT calculation, revealing an evident $J_{\rm eff} = 1/2$ character. A clear separation between the $J_{\rm eff} = 1/2$ and 3/2 states with the gap opening can be seen, showing that the enhancement of the $J_{\rm eff} = 1/2$ - 3/2 splitting by electron correlations is significant even in the paramagnetic phase. This explains a schematic energy level diagram shown in Fig. 4b). It is worth mentioning that such noticeable enhancement of SOC has not been observed in previous nonmagnetic DFT+U results (see the left panel of Fig. 4c)).[31,57,59,60]

At high pressure, it was sufficient to perform DFT calculations to describe the electronic structure possibly because the correlation effects become less important in the dimerized monoclinic structure. The optimized monoclinic crystal structure, starting from the experimentally-determined monoclinic structure[31], is visualized in Fig. 4d), where the bond lengths for the short (thick orange lines) and long Ir-Ir bonds (thin dark and light blue lines) are 2.60 and 3.05 Å. In Fig. 4d), we also depicted the black solid box for the monoclinic unit cell at high pressure, where one can compare with the orthorhombic unit cell at ambient pressure in Fig. 4a) by finding how the Ir dimers are formed at high pressure using an inset. This strong Ir dimerization found in the DFT-optimized structure is consistent with the experimental observation using x-rays[31]; 2.662 and 3.012 Å for the short and long Ir-Ir bonds respectively. This imposes a large ligand field to the Ir t_{2g} orbitals.

Figure 4e) sketches the energy level splitting within the Ir t_{2g} dimer, where the DFT-calculated PDOS is shown in Fig. 4f). The results clearly demonstrate an energy gap associated with a strong bonding-antibonding splitting within the t_{2g} states, rendering the SOC ineffective and converting monoclinic β-Li_2IrO_3 into a non-magnetic band insulator. These results are consistent with a recent resonant inelastic x-ray scattering that also indicate the pressure-induced breakdown of the spin-orbit Mott insulating state in β-Li_2IrO_3[43] and the DFT theory.[61].

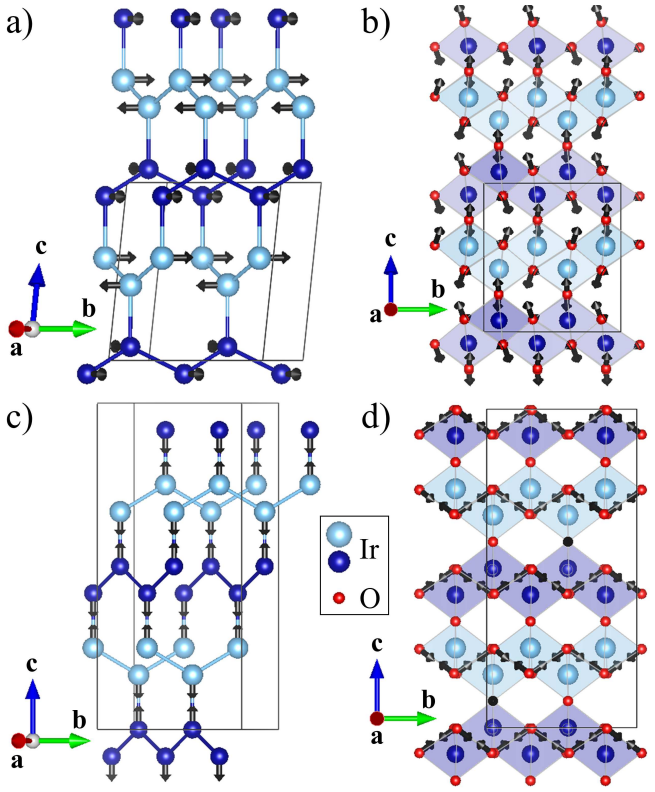

FIG. 5. (color online) Comparison between the eigenvectors of representative phonons at both ambient and high pressure. Calculated Raman-active A_g vibrations at high pressure in a) and b) and at ambient pressure in c) and d) are compared in the spectral ranges most affected by the structural transition. Two sets of calculated Raman mode are visualized and compared. A lower-energy Raman-active vibration is illustrated in a) 152 cm^{-1} at high pressure, which is compared with c) 194 cm^{-1} at ambient pressure. Similarly, a higher-energy Raman vibration is shown in b) 579 cm^{-1} at high pressure, which is compared with d) 587 cm^{-1} at ambient pressure. Atomic vibrations from Li and O (Ir and Li) ions are hardly seen in a) and c) (b) and d)) owing to the large differences in masses of ions. Smaller red balls are for oxygen ions.

C. Comparison between experimental and computational data

We are now in a position to compare our experimental and theoretical data. At ambient pressure, we experimentally observe nearly all predicted phonons, and the frequencies agree reasonably well with the calculations (see Fig. 1 and Tables I and II for comparison). On the other hand, a similar comparison is not possible in the high pressure phase due to the low symmetry of the lattice and the large number of phonon modes observed. However, the measured Raman spectra can be qualitatively understood by relating the data from ambient to high pressure to the underlying crystal structures.

Specifically, we compared experimental and computational data of representative phonons in the highlighted regions of wavenumbers at around 150 and 550 cm^{-1} in Fig. 2a). At ambient pressure, we examined two Raman-active phonons illustrated in Fig. 5c) and d) with calculated frequencies of 194 cm^{-1} and 587 cm^{-1} (see Table I for a list of Raman-active phonons calculated for comparison with the experimental list in Table II). The eigenvectors are dominated by Ir vibrations at the lower frequency (due to heavier masses) and oxygen vibrations at the higher frequency (due to lighter masses).

At high pressure, the strong dimerization of Ir bonds and the corresponding distortion of oxygen octahedral cages [as visualized in Fig. 4b)] are expected to greatly affect the phonon modes. For instance, the dimerized bond of Ir ions (the heaviest ions) is anticipated to alter mostly the low-energy Raman spectra, and indeed we observed a significant modification of the phonon spec-

TABLE I. Calculated Raman-active phonons by VASP for ambient orthorhombic and high-pressure monoclinic crystal structure with an unit of cm^{-1}.

	$A_g(1)$	$A_g(2)$	$A_g(3)$	$A_g(4)$	$A_g(5)$	$A_g(6)$	$A_g(7)$		
A_g (Fddd)	194	281	326	342	503	516	587		
	$B_{1g}(1)$	$B_{1g}(2)$	$B_{1g}(3)$	$B_{1g}(4)$	$B_{1g}(5)$	$B_{1g}(6)$	$B_{1g}(7)$	$B_{1g}(8)$	
B_{1g} (Fddd)	141	2588	274	332	359	500	550	604	
	$A_g(1)$	$A_g(2)$	$A_g(3)$	$A_g(4)$	$A_g(5)$	$A_g(6)$	$A_g(7)$	$A_g(8)$	$A_g(9)$
A_g (C2/c)	152	215	251	255	278	314	344	360	388
	$A_g(10)$	$A_g(11)$	$A_g(12)$	$A_g(13)$	$A_g(14)$	$A_g(15)$	$A_g(16)$	$A_g(17)$	$A_g(18)$
	395	470	477	519	534	571	579	605	701

tra between 100 $\sim$ 200 cm^{-1}. This is, in turn, confirmed by the Ir-dominant atomic vibrations (with negligible amount of Li and O vibrations) found in the DFT-calculated A_g-phonon modes as compared in Fig. 5c) (at 194 cm^{-1} from Fddd) and 5a) (at 152 cm^{-1} from C2/c) for the ambient and high pressure, respectively. Also, a similarly sudden change of the phonon spectra at high pressure was seen at higher-energy, which should be naturally linked to the lighter oxygen ions. Indeed, this can be seen from the DFT phonon modes shown in Fig. 5d) (at 587 cm^{-1} from Fddd, the highest A_g-mode calculated) and 5b) (at 579 cm^{-1} from C2/c)

We should note that these vibrations are qualitatively distinct even though they have similar frequencies: their eigenvectors are almost perpendicular to each other as shown in Fig. 5a) and 5c), and 5b) and 5d). We confirmed that two phonon modes calculated at high pressure (Fig. 5a) and Fig. 5b)) are not present among the calculated Raman modes at ambient pressure. In short, both the Raman experiments and the phonon calculations reveal the distinct nature of the atomic motions in ambient and high-pressure structures.

Our results fit into a conceptual framework that attributes a variety of related phenomena in 4d- and 5d-electron materials to a competition between intermetallic covalency and magnetism.[62] Within this framework, the formation of dimerized bonds can be understood as a consequence of the reduced kinetic energy of the electrons within the dimer at the expense of the formation of localized magnetic moments. Our observations in β-Li_2IrO_3 under pressure are consistent with the notion that the shrinking of Ir - Ir distances with pressure sharply increases the hopping between d - d orbitals, driving a first-order structural transition. This theory[62] has also been applied to 3d transition metal compounds such as CrO_2,[63] where a dimerized monoclinic structure is theoretically predicted at about 70 GPa.[62,63] The lower critical pressure in β-Li_2IrO_3 may be due to the much more extended 5d orbitals with the larger d - d hopping compared to its 3d counterpart. These considerations can be generalized to the family of α, β, γ-Li_2IrO_3 based on similar observations. For example, high-pressure resonant inelastic x-ray scattering experiments on α-Li_2IrO_3[28] have observed the breakdown of the $J_{\text{eff}} = 1/2$ picture between 0.1 GPa and 2 GPa, followed by a structural transition to the dimerized ground state at above 3 GPa.

V. SUMMARY

We performed a combined analysis using high-pressure Raman scattering and *ab-initio* calculations on the hyperhoneycomb iridate β-Li_2IrO_3. Using Raman scattering under pressure, we experimentally observed the broadening and splitting of phonon peaks and the appearance of new modes at high pressure, explained by a symmetry lowering via a first-order structural transition. This is further confirmed by phonon calculations comparing the lattice dynamics at both pressures. The calculations clearly demonstrated the breakdown of the $J_{\text{eff}} = 1/2$ state due to the Ir-Ir bond dimerization that leads to the high-pressure monoclinic phase. This observation can be interpreted in terms of a competition between intermetallic covalency and the formation of Ir local moments. Our results demonstrate that Raman scattering is an effective probe of pressure-induced structural and electronic phase transitions in materials with 4d and 5d valence electrons.

VI. ACKNOWLEDGEMENTS

We appreciate technical support from Jürgen Nuss for x-ray characterization to cross-check the orientation of crystals, from Uwe Engelhardt for preparing high-pressure gaskets, and especially from Karl Syassen for providing the diamond anvil cell and helping to mount crystals as well as from Junhong Na for helping Raman

measurements. H.-S. K. thanks Cyrus Dreyer for providing his script on phonon mode projections. We acknowledge funding from the Deutsche Forschungsgemeinschaft (DFG, German Research Foundation) – Projektnummer 107745057 – TRR 80. H.-S. K., K. H., and D. V. are supported by NSF DMREF grant DMR-1629059.

* Present address: Rutgers Center for Emergent Materials and Department of Physics and Astronomy, Rutgers University, Piscataway, New Jersey 08854, USA; sc1853@physics.rutgers.edu

[1] W. Witczak-Krempa, G. Chen, Y. B. Kim, L. Balents, Annu. Rev. Condens. Matter Phys. **5**, 57 (2014).

[2] A. Kitaev, Ann. Physics **321**, 2 (2006).

[3] J. Chaloupka, G. Jackeli, and G. Khaliullin, Phys. Rev. Lett. **105**, 027204 (2010).

[4] G. Jackeli, and G. Khaliullin, Phys. Rev. Lett. **102**, 017205 (2009).

[5] S. Mandal and N. Surendran, Phys. Rev. B **79**, 024426 (2009).

[6] E. K. Lee, R. Schaffer, S. Bhattacharjee, and Y. B. Kim, Phys. Rev. B **89**, 045117 (2014).

[7] I. Kimchi, R. Coldea, and A. Vishwanath, Phys. Rev. B **91**, 245134 (2015).

[8] Y. Singh, and P. Gegenwart, Phys. Rev. B **82**, 064412 (2010); Y. Singh, S. Manni, J. Reuther, T. Berlijn, R. Thomale, W. Ku, S. Trebst, and P. Gegenwart, Phys. Rev. Lett. **108**, 127203 (2012).

[9] T. Takayama, A. Kato, R. Dinnebier, J. Nuss, H. Kono, L. S. I. Veiga, G. Fabbris, D. Haskel, and H. Takagi, Phys. Rev. Lett. **114**, 077202 (2015).

[10] K. A. Modic, T. E. Smidt, I. Kimchi, N. P. Breznay, A. Biffin, S. Choi, R. D. Johnson, R. Coldea, P. Watkins-Curry, G. T. McCandless, J. Y. Chan, F. Gandara, Z. Islam, A. Vishwanath, A. Shekhter, R. D. McDonald, and J. G. Analytis, Nat. Commun. **5**, 4203 (2014).

[11] K. W. Plumb, J. P. Clancy, L. J. Sandilands, V. V. Shankar, Y. F. Hu, K. S. Burch, H.-Y. Kee, and Y.-J. Kim, Phys. Rev. B **90**, 041112 (2014).

[12] F. Ye, S. Chi, H. Cao, B. C. Chakoumakos, J. A. Fernandez-Baca, R. Custelcean, T. F. Qi, O. B. Korneta, and G. Cao, Phys. Rev. B **85**, 180403 (2012).

[13] S. K. Choi, R. Coldea, A. N. Kolmogorov, T. Lancaster, I. I. Mazin, S. J. Blundell, P. G. Radaelli, Y. Singh, P. Gegenwart, K. R. Choi, S.-W. Cheong, P. J. Baker, C. Stock, and J. Taylor, Phys. Rev. Lett. **108**, 127204 (2012).

[14] X. Liu, T. Berlijn, W. G. Yin, W. Ku, A. Tsvelik, Y.-J. Kim, H. Gretarsson, Y. Singh, P. Gegenwart, and J. P. Hill, Phys. Rev. B **83**, 220403 (2011).

[15] S. Chun, J.-W. Kim, J. Kim, H. Zheng, C. C. Stoumpos, C. D. Malliakas, J. F. Mitchell, K. Mehlawat, Y. Singh, Y. Choi, T. Gog, A. Al-Zein, M. M. Sala, M. Krisch, J. Chaloupka, G. Jackeli, G. Khaliullin, and B. J. Kim, Nat. Phys. **11** 462 (2015).

[16] R. D. Johnson, S. C. Williams, A. A. Haghighirad, J. Singleton, V. Zapf, P. Manuel, I. I. Mazin, Y. Li, H. O. Jeschke, R. Valentí, and R. Coldea, Phys. Rev. B **92**, 235119 (2015).

[17] A. Banerjee, C. A. Bridges, J.-Q. Yan, A. A. Aczel, L. Li, M. B. Stone, G. E. Granroth, M. D. Lumsden, Y. Yiu, J. Knolle, S. Bhattacharjee, D. L. Kovrizhin, R. Moessner, D. A. Tennant, D. G. Mandrus, and S. E. Nagler, Nat. Mater. **15**, 733 (2016).

[18] A. Biffin, R. D. Johnson, S. Choi, F. Freund, S. Manni, A. Bombardi, P. Manuel, P. Gegenwart, and R. Coldea, Phys. Rev. B **90**, 205116 (2014).

[19] A. Biffin, R. D. Johnson, I. Kimchi, R. Morris, A. Bombardi, J. G. Analytis, A. Vishwanath, and R. Coldea, Phys. Rev. Lett. **113**, 197201 (2014).

[20] S. C. Williams, R. D. Johnson, F. Freund, S. Choi, A. Jesche, I. Kimchi, S. Manni, A. Bombardi, P. Manuel, P. Gegenwart, and R. Coldea, Phys. Rev. B **93**, 195158 (2016).

[21] S. Choi, S. Manni, J. Singleton, C.V. Topping, T. Lancaster, S.J. Blundell, D.T. Adroja, V. Zapf, P. Gegenwart, R. Coldea, Phys. Rev. B **99**, 054426 (2019).

[22] E. K.-H. Lee, J. G. Rau, and Y. B. Kim, Phys. Rev. B **93**, 184420 (2016).

[23] M. W. Stephen, A. T. Alexander, D. Maria, B. J. van den, S. Yogesh, G. Philipp, and V. Roser, J. Phys. Condens. Matter **29**, 493002 (2017).

[24] V. M. Katukuri, S. Nishimoto, V. Yushankhai, A. Stoyanova, H. Kandpal, S. Choi, R. Coldea, I. Rousochatzakis, L. Hozoi, and J. van den Brink, New J. Phys. **16**, 013056 (2014).

[25] V. Hermann, J. Ebad-Allah, F. Freund, I. M. Pietsch, A. Jesche, A. A. Tsirlin, J. Deisenhofer, M. Hanfland, P. Gegenwart, and C. A. Kuntscher, Phys. Rev. B **96**, 195137 (2017).

[26] G. Simutis, N. Barbero, K. Rolfs, P. Leroy-Calatayud, K. Mehlawat, R. Khasanov, H. Luetkens, E. Pomjakushina, Y. Singh, H.-R. Ott, J. Mesot, A. Amato, and T. Shiroka, Phys. Rev. B **98**, 104421 (2018).

[27] M. A. V. Hermann, J. Ebad-Allah, F. Freund, A. Jesche, A. A. Tsirlin, M. Hanfland, P. Gegenwart, I. I. Mazin, D. I. Khomskii, R. Valentí, and C. A. Kuntscher, Phys. Rev. B **97**, R020104 (2018).

[28] J. P. Clancy, H. Gretarsson, J. A. Sears Y. Singh, S. Desgreniers, K. Mehlawat, S. Layek, G. Kh. Rozenberg, Y. Ding, M. H. Upton, D. Casa, N. Chen, J. Im, Y. Lee, R. Yadav, L. Hozoi, D. Efremov, J. van den Brink, and Y.-J. Kim, npj Quantum Materials **3**, 35 (2018).

[29] V. Hermann, J. Ebad-Allah, F. Freund, A. Jesche, A. A. Tsirlin, P. Gegenwart, and C. A. Kuntscher, Phys. Rev. B **99**, 235116 (2019).

[30] M. Majumder, R. S. Manna, G. Simutis, J. C. Orain, T. Dey, F. Freund, R. K. A. Jesche, P.K. Biswas, E. Bykova, N. Dubrovinskaia, L.S. Dubrovinsky, L. H. R. Yadav, S. Nishimoto, A.A. Tsirlin, and P. Gegenwart, Phys. Rev. Lett. **120**, 237202 (2018).

[31] L. S. I. Veiga, M. Etter, K. Glazyrin, F. Sun, C. A. Escanhoela, Jr. G. Fabbris, J. R. L. Mardegan, P. S. Malavi, Y. Deng, P. P. Stavropoulos, H.-Y. Kee, W. G. Yang, M. van Veenendaal, J. S. Schilling, T. Takayama, H. Takagi, and D. Haskel, Phys. Rev. B **96**, 140402(R) (2017).

[32] L. S. I. Veiga, K. Glazyrin, G. Fabbris, C. D. Dashwood, J. G. Vale, H. Park, M. Etter, T. Irifune, S. Pascarelli, D. F. McMorrow, T. Takayama, H. Takagi, D. Haskel, https://arxiv.org/abs/1905.08211 (2019).

TABLE II. Peak positions extracted from the fit using the green Raman data collected upon pressure for four polarizations as shown in Fig. 2. The unit of frequencies is cm^{-1}.

$\bar{c}(\boldsymbol{aa})\boldsymbol{c}$ P (GPa)	-	-	$A_g(1)$	-	-	-	$A_g(2)$	-	-	-	-	$A_g(4)$	$A_g(6)$	$A_g(7)$
0	-	-	188	-	-	-	330	-	-	-	-	518	596	661
0	-	-	188	-	-	-	330	-	-	-	-	520	596	663
2.4	-	-	159	-	-	-	-	-	-	-	-	533	606	688
3	-	-	156	-	-	-	-	-	-	-	-	536	619	668
$P>P_c$	$A_g^*(1)$	$A_g^*(2)$	$A_g^*(3)$	$A_g^*(4)$	$A_g^*(5)$	$A_g^*(6)$	$A_g^*(7)$	$A_g^*(8)$	$A_g^*(9)$	$A_g^*(10)$	$A_g^*(11)$	$A_g^*(12)$	$A_g^*(13)$	$A_g^*(14)$
4.53	143	164	189	-	-	-	-	392	434	536	566	-	635	672
5	143	164	189	-	-	-	-	392	434	536	566	601	635	672
6.3	144	163	184	200	-	-	-	401	455	556	579	607	673	687
7.62	149	163	189	203	-	-	-	405	467	562	585	613	687	697
$\bar{c}(\boldsymbol{bb})\boldsymbol{c}$ P (GPa)	-	-	$A_g(1)$	-	-	-	$A_g(2)$	-	-	-	-	$A_g(4)$	$A_g(6)$	$A_g(7)$
0	-	-	187	-	-	-	357	-	-	-	-	519	596	665
0	-	-	183	-	-	-	357	-	-	-	-	520	598	672
2.4	-	-	148	-	-	-	356	-	-	-	-	530	621	667
3	-	-	150	-	-	-	375	-	-	-	-	533	630	670
$P>P_c$	$A_g^*(1)$	$A_g^*(2)$	$A_g^*(3)$	$A_g^*(4)$	$A_g^*(5)$	$A_g^*(6)$	$A_g^*(7)$	$A_g^*(8)$	$A_g^*(9)$	$A_g^*(10)$	$A_g^*(11)$	$A_g^*(12)$	$A_g^*(13)$	$A_g^*(14)$
4.53	118	139	164	184	-	-	-	388	434	547	561	-	637	669
5	135	159	179	196	-	-	-	394	443	552	573	-	642	675
6.3	143	163	187	201	-	280	-	401	463	558	582	-	645	681
7.62	150	168	195	205	-	284	-	405	-	565	591	-	-	-
$\bar{c}(\boldsymbol{ab})\boldsymbol{c}$ P (GPa)	-	-	$B_{1g}(1)$	-	$B_{1g}(4)$	-	$B_{1g}(5)$	-	$B_{1g}(6)$	-	-	$B_{1g}(7)$	-	$B_{1g}(8)$
0	-	-	153	-	-	-	380	-	522	-	-	559	-	625
0	-	-	151	-	319	-	360	-	520	-	-	569	-	627
2.4	-	-	157	-	-	-	-	-	534	-	-	609	-	677
3	-	-	157	-	-	-	-	-	539	-	-	613	-	685
$P>P_c$	$A_g^*(1)$	$A_g^*(2)$	$A_g^*(3)$	$A_g^*(4)$	$A_g^*(5)$	$A_g^*(6)$	$A_g^*(7)$	$A_g^*(8)$	$A_g^*(9)$	$A_g^*(10)$	$A_g^*(11)$	$A_g^*(12)$	$A_g^*(13)$	$A_g^*(14)$
4.53	122	155	165	180	-	-	-	394	-	535	560	607	624	674
5	127	147	178	195	-	278	-	398	-	555	572	602	645	681
6.3	130	149	187	200	-	282	-	403	-	564	583	611	656	694
7.62	149	166	187	200	-	282	-	403	-	566	586	613	661	698
$\bar{c}(\boldsymbol{ba})\boldsymbol{c}$ P (GPa)	-	-	$B_{1g}(1)$	-	$B_{1g}(4)$	-	$B_{1g}(5)$	-	$B_{1g}(6)$	-	-	$B_{1g}(7)$	-	$B_{1g}(8)$
0	-	-	152	-	323	-	367	-	501	-	-	557	-	629
0	-	-	152	-	314	-	363	-	500	-	-	561	-	630
2.4	-	-	160	-	-	-	-	-	533	-	-	607	-	672
3	-	-	161	-	-	-	-	-	533	-	-	609	-	686
$P>P_c$	$A_g^*(1)$	$A_g^*(2)$	$A_g^*(3)$	$A_g^*(4)$	$A_g^*(5)$	$A_g^*(6)$	$A_g^*(7)$	$A_g^*(8)$	$A_g^*(9)$	$A_g^*(10)$	$A_g^*(11)$	$A_g^*(12)$	$A_g^*(13)$	$A_g^*(14)$
4.53	130	144	165	182	-	-	-	392	-	532	563	604	637	676
5	139	158	177	189	-	279	-	394	-	553	570	603	643	681
6.3	150	161	184	200	-	279	-	401	-	563	579	609	663	693
7.62	152	165	188	203	-	283	-	404	-	567	584	614	660	697

[33] A. Ruiz, A. Frano, N. P. Breznay, I. Kimchi, T. Helm, I. Oswald, J. Y. Chan, R. J. Birgeneau, Z. Islam, and J. G. Analytis, Nat. Commun. **8**, 961 (2017).

[34] N. P. Breznay, A. Ruiz, A. Frano, W. Bi, R. J. Birgeneau, D. Haskel, and J. G. Analytis, Phys. Rev. B **96**, R020402 (2017).

[35] R. Yadav, S. Rachel, L. Hozoi, J. van den Brink, and G. Jackeli, Phys. Rev. B **98**, R121107 (2018).

[36] T. Biesner, S. Biswas, W. Li, Y. Saito, A. Pustogow, M. Altmeyer, A. U. B. Wolter, B. Büchner, M. Roslova, T. Doert, S. M. Winter, R. Valentí, and M. Dressel, Phys. Rev. B **97**, R220401 (2018).

[37] G. Garbarino, R. Yadav, F. J. Martinez-Casado, R. Beltrán Rodríguez, Q. Stahl, M. Kusch, S. P. Limandri, R. Ray, P. Lampen-Kelley, D. G. Mandrus, S. E. Nagler, M. Roslova, A. Isaeva, T. Doert, L. Hozoi, A. U. B. Wolter, B. Büchner, J. Geck, and J. van den Brink, Phys. Rev. B **97**, R241108 (2018).

[38] G. Li, X. Chen, Y. Gan, F. Li, M. Yan, F. Ye, S. Pei, Y. Zhang, L. Wang, H. Su, J. Dai, Y. Chen, Y. Shi, X. Wang, L. Zhang, S. Wang, D. Yu, F. Ye, J.-W. Mei, and M. Huang, Phys. Rev. Mater. **3**, 023601 (2019).

[39] K. Kitagawa, T. Takayama, Y. Matsumoto, A. Kato, R. Takano, Y. Kishimoto, S. Bette, R. Dinnebier, G. Jackeli, H. Takagi, Nature **554**, 341 (2018).

[40] K. Hu, Z. Zhou, Y.-W. Wei, C.-K. Li, and J. Feng, Phys. Rev. B **98**, 100103 (2018).

[41] M. Taheri, F. S. Razavi, Z. Yamani, R. Flacau, P. G. Reuvekamp, A. Schulz, and R. K. Kremer, Phys. Rev. B **93**, 104414 (2016); G. Han, S. Choi, H. Cho, B. Sohn, J.-G. Park, and C. Kim, Phys. Rev. B **98**, 125114 (2018).

[42] F. Freund, S. C. Williams, R. D. Johnson, R. Coldea, P. Gegenwart, and A. Jesche, Sci. Rep. **6**, 35362 (2016).

[43] T. Takayama, A. Krajewska, A. S. Gibbs, A. N. Yaresko, H. Ishii, H. Yamaoka, K. Ishii, N. Hiraoka, N. P. Funnell, C. L. Bull, H. Takagi, Phys. Rev. B **99**, 125127 (2019).

[44] A. Glamazda, P. Lemmens, S.-H. Do, Y. S. Choi, and K.-Y. Choi, Nat. Commun. **7**, 12286 (2016).

[45] U. Fano, Phys. Rev. **124**, 1866 (1961).

[46] T. C. Damen, S. P. S. Porto, and B. Tell, Phys. Rev. **142**, 570 (1966).

[47] Supplemental Material is given at http://link.aps.org/supplemental/... (this address will be given by APS later) for full technical details such as single crystal growth and characterization, Raman measurements to characterize beam-heating, high-pressure Raman measurements, and computations. DFT/DMFT-optimized crystal structures are also included.

[48] S. Klotz, L. Paumier, G. Le March, and P. Munsch, High Press Res **29**, 649 (2009).

[49] K. Syassen, High Press Res **28**, 75 (2008).

[50] G. Kresse, and J. Furthmüller, Phys. Rev. B **54**, 11169 (1996).

[51] G. Kresse, and D. Joubert, Phys. Rev. B **59**, 1758 (1999).

[52] P. Blaha, K. Schwarz, G. K. H. Madsen, D. Kvasnicka, and J. Luitz, *WIEN2k, An Augmented Plane Wave + Local Orbitals Program for Calculating Crystal Properties* (Karlheinz Schwarz, Techn. Universität Wien, Austria, 2001).

[53] http://hauleweb.rutgers.edu/tutorials/

[54] K. Haule, C.-H. Yee, and K. Kim, Phys. Rev. B **81**, 195107 (2010).

[55] K. Haule, J. Phys. Soc. Jpn. **87**, 041005 (2018).

[56] A. Togo and I. Tanaka, Scr. Mater. **108**, 1 (2015).

[57] H.-S. Kim, Y. B. Kim, and H.-Y. Kee, Phys. Rev. B **94**, 245127 (2016).

[58] See Supplemental Material[47] for a discussion of the mismatch of Raman frequencies in calculations and experiments.

[59] E. K.-H. Lee, S. Bhattacharjee, K. Hwang, H.-S. Kim, H. Jin, and Y. B. Kim, Phys. Rev. B **89**, 205132 (2014).

[60] H.-S. Kim, E. K.-H. Lee, and Y. B. Kim, EPL **112**, 67004 (2015).

[61] V. N. Antonov, S. Uba, and L. Uba, Phys. Rev. B **98**, 245113 (2018).

[62] S. V. Streltsov, and D. I. Khomskii, PNAS, **113**, 10491 (2016).

[63] S. Kim, K. Kim, C.-J. Kang, and B. I. Min, Phys. Rev. B **85**, 094106 (2012).